Article

Novel Heterostructures of Noble Plasmonic Metals/Ga-Substituted Hydrotalcite for Solar Light Driven Photocatalysis toward Water Purification

Eugenia Corina Ignat [1], Doina Lutic [2,*], Gabriel Ababei [3] and Gabriela Carja [1,*]

[1] Department of Chemical Engineering, Faculty of Chemical Engineering and Environmental Protection "Cristofor Simionescu", Technical University of Iasi, 71 D. Mangeron, 700050 Iasi, Romania
[2] Faculty of Chemistry, Al. I. Cuza University of Iasi, 11 Bd. Carol I, 700501 Iasi, Romania
[3] National Institute of Research and Development for Technical Physics, 47 Mangeron Boulevard, 700050 Iasi, Romania
* Correspondence: doilub@uaic.ro (D.L.); carja@uaic.ro (G.C.); Tel./Fax: +40-740-23-6565 (D.L.); +40-232-20-1231 (G.C.)

Abstract: Heterostructures formed by close conjunctions of plasmonic metal nanoparticles and non-plasmonic (2D) lamellar nanostructures are receiving extensive interest as solar-light-driven photocatalysts for environmental pollutant remediation. Herein, the conjunction of plasmonic Au or Ag and Ga-substituted hydrotalcite are obtained by exploiting the manifestation of the structural "memory effect" of Ga-substituted hydrotalcite in the aqueous solutions of $Au(CH_3COO)_3$ and Ag_2SO_4, respectively. The 2D layered matrix of MgGaAl plays a dual function; it is involved in the synthesis of the plasmonic metal nanoparticles, and further, is acting as a support. The compressive investigations using X-ray diffraction (XRD), UV-diffuse reflectance spectroscopy (UVDR), infrared spectroscopy (FT-IR), transmission electron microscopy (TEM/HRTEM), high-angle annular dark-field imaging/scanning transmittance electron microscopy (HAADF/STEM) and X-ray photoelectron spectroscopy (XPS) describe structural, composition and nano/micromorphology characteristics of the novel heterostructures, while UVDR analysis afforded to study the features of their plasmonic responses. Results reveal that the catalysts are formed by close conjunction of small nanoparticles of Au or Ag (with a mean size less than 20 nm) that are formed on the larger particles of MgGaAl and own plasmonic features within the visible range. The catalysts performances were tested towards photocatalytic degradation of p-dichlorobenzene and 4-nitrophenol under solar light irradiation. Results revealed that the degradation of the pollutants is entangled to the plasmonic response of the heterostructured catalysts that is the key functionality in promoting photocatalysis and degrading the pollutants, under solar light irradiation. MgGaAl showed a very low photocatalytic activity when irradiated by UV or solar light. Notably, the heterostructured catalysts proceeded in good to excellent yield to remove the tested pollutants, under solar light irradiation. The sustainability of the novel catalysts was assessed through the kinetic analysis of the degradation processes of the tested pollutants and their mixture.

Keywords: layered double hydroxides; plasmonic metals; solar light photocatalysis

1. Introduction

Deterioration of the environment and a shortage of sustainable energy supply have become major societal issues that are threating the development of human society and the preservation of our planet [1]. Whereas water shortage was for many decades associated to certain regions from Africa and central Asia, nowadays becomes a worrying problem worldwide, being entangled to the climate changes from the last decades [2]. Nowadays a large variety of organic pollutants have been found in effluents of sewage treatment plants, rivers, surface and ground waters [3]. Among them, man-made consumables containing

phenols, dyes, nitrobenzene or halobenzene compounds are the leading sources of water pollution [4]. The quest to provide clean water has led to a tremendous boost in the scientific efforts to develop novel performant technologies for environmental remediation [5]. Toward this, photocatalysis has received much attention because, among the traditional physical techniques, it provides a powerful tool for the removal of organic contaminants by completely degrading them [6]. Inside this, solar-light-driven photocatalysis is an effective and very promising way to meet both energy demands and water pollution issues [7]. It utilizes photogenerated carriers (electrons and holes) to initiate redox reactions and realize solar-to-chemical energy conversion.

The demonstrations of solar-light-driven chemical transformations on plasmonic nanostructures have led to the emergence of a new field in heterogeneous catalysis known as plasmonic catalysis [8]. Plasmonic metals are light-harvesting nanostructures that interact with visible light through the excitation of localized surface plasmon resonance (LSPR) [9]. A question that has emerged recently is whether it is possible to take advantage of the functionality of the plasmonic behavior in multicomponent catalysts. These are formed by close conjunctions of a plasmonic metal, which amplifies and concentrates the photons' energy within the material and, a non-plasmonic component that is able to play the role of support to stabilize the nanometal and, further, to extract the plasmon energy in the form of electronic excitations to perform a targeted catalytic function [10]. On such a plasmonic/non-plasmonic interface the light energy harvested by the plasmonic metal can modulate specific interactions with the support that are entangled to the rearrangement of electrons, transfer of photogenerated carriers and their prolonged lifetime and the extended light-response range within heterostructured components [11].

LDH are 2D layered matrices with a brucite-like structure that are conventionally described by the general formula $[M^{II}_{1-x}M^{III}_x(OH)_2]^{x+} \cdot A^{n-}_{x/n} \cdot mH_2O$, where the divalent M^{II} and trivalent M^{III} cations might be defined as Mg^{2+}, Zn^{2+}, Cu^{2+}, Al^{3+}, Ga^{3+}, etc. and, the A^{n-} can be almost any organic or inorganic anion [12]. The possibility to incorporate specific cations in the 2D layers of LDH delivers a generous palette of semi-conductive materials useful for photocatalytic devices [13–15]. Further, LDH are relatively simple and cheap to prepare and own the ability to reconstruct its layered structure when the calcined LDH are introduced in the aqueous solutions containing anions [16,17]. By virtue of their unique 2D-layered structure, tuned optical absorption, their hydroxylated surfaces and ease of preparation, LDHs have emerged as very promising candidates for obtaining versatile and robust catalysts for many actual and potential applications and several reviews on this topic are available [18–25]. Importantly, the close conjunction of the LDH matrix and plasmonic nanoparticles affords to obtain multicomponent catalysts in which the LDH unit plays multifarious roles including immobilization and stabilization of nanoparticles [26], and further provides a unique interface-space confined in a 2D matrix for controlling nanoparticle spatial distribution [27]. Additionally, serving as a support, LDH will afford to stabilize low nuclearity nanospecies on its surface by minimizing atom diffusion, controlling the nanoparticle morphology and tuning active nanometal electronic structure [28].

4-Nitrophenol (4-NPh) is one of the highly toxic organic pollutants found among the substances bearing nitro groups, which are common components of industrial effluents. It has been detected in urban and agricultural waste and is recognized as a priority hazardous pollutant by the Environmental Protection Agency (EPA) due to its poisonous and volatile nature. [29]. Furthermore, para-Dichlorobenzene (p-DCB) is the main component of moth balls, disinfection fumigants and toilet deodorization cakes. It is considered a low toxicity compound, but it causes skin, eyes and gastrointestinal tract irritation, causing nausea, vomiting and diarrhea. Neurotoxic effects (retardation, dysarthria, ataxia, cognitive decline, memory disorders) were reported in cases of ingestion [30].

Herein, by exploiting the "structural reconstruction" of the LDH in the aqueous solutions of $Au(CH_3COO)_2$ and Ag_2SO_4, respectively, we successfully constructed novel plasmonic heterostructures defined by the close conjunction of nanoparticles of Au or Ag

with gallium partially substituted hydrotalcite-like 2D matrix, denoted as Au_MgGaAl and Ag_MgGaAl, respectively. Next, we present their structural, morphological and plasmonic characteristics and applications in plasmon-induced photocatalysis toward degradation of both 4-NPh and p-DCB from water. Results point out the enhanced catalytic performances of the synthesized plasmonic heterostructures in comparison to their calcined forms and the basic LDH, and further reveal the advantage of plasmonic metals in catalyst composition. A discussion of the kinetic models that govern the studied plasmonic catalysis is also included.

2. Results and Discussion

2.1. Synthesis Procedures and Structure Characterization

In our method, MgGaAl was obtained by coprecipitation at constant pH and 65 °C, while Ag_MgGaAl and Au_MgGaAl were obtained, at room temperature, after the reconstruction of the calcined MgGaAl in the aqueous solutions of $Au(CH_3COO)_3$ and Ag_2SO_4, respectively [31]. In fact, the synthesis procedures exploited the LDH capability to manifest its structural memory in the aqueous solution containing CH_3COO^- and SO_4^{2-} [31]. The purities and crystalline phases of the as-prepared samples were analyzed by X-ray diffraction (XRD). Figure 1a shows the XRD diffractograms of MgGaAl as "as synthesized" and after the reconstruction processes. The recovery of the LDH structure by reconstruction is shown by the XRD analysis, revealing patterns that could be perfectly indexed to the LDHs phase (ICDD file No. 22-700), with a series of sharp and symmetric basal reflections of the (00ℓ, $\ell = 3, 6, 9$) planes and broad, less intense, reflections for the nonbasal (01ℓ, $\ell = 2,5,8$) planes [32]. Particularly, MgGaAl shows a well crystalized LDH structure though, other phases such as gallium oxy-hydroxide GaOOH are easily identified, as indicated as their characteristic reflections at $2\theta = 34.5, 39$ and 46.88 (JCPDS file no. 36-1451) denoted in Figure 1a as (*). Importantly, after the reconstruction, the structural features of Ag_MgGaAl and Au_MgGaAl are defined as a single crystalline LDH-like phase, pointing out that the reconstruction procedure, at ambient temperature, promoted the reconstruction of the LDH.
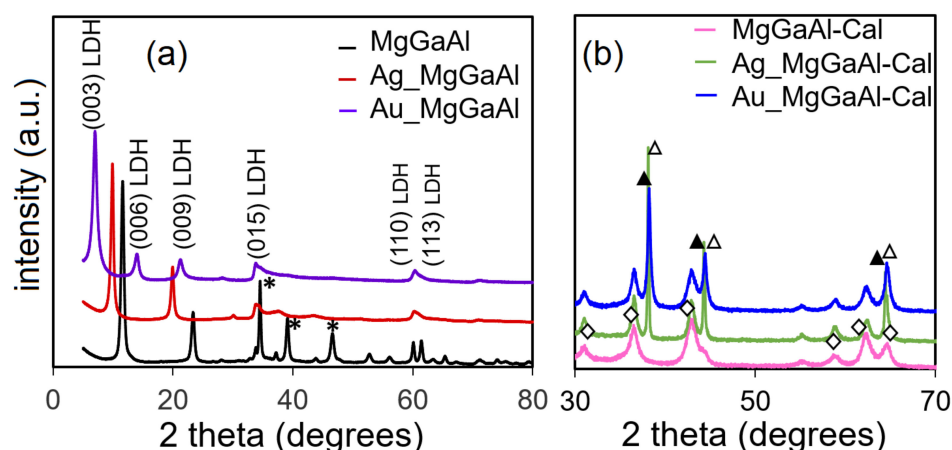

Figure 1. XRD patterns of (**a**). MgGaAl, Ag_MgGaAl and Au_MgGaAl; (**b**) after calcination at 870 °C. (*) GaOOH; Δ Au and ▲ Ag; ◇ $MgGa_2O_4$.

The most intense peak corresponds to (003) reflection and is associated with the distance between two consecutive brucite-like layers in the LDH structure. On the contrary, for Ag_MgGaAl and Au_MgGaAl the position of (003) reflection shifted to lower 2θ degrees. The (003) peak is related to the interlayer distance between the brucite-like layers that is established by the size of the anions of the interlayers and the 2θ values of (003), which are 11.52°, 9.92° and 6.94° for MgGaAl, Ag_MgGaAl and Au_MgGaAl, respectively. This shows that the reconstruction process altered the LDH interlayer space. Therefore, the replacement of carbonate anions of MgGaAl with the acetate and sulfate anions, after the reconstruction, promoted the increase of the interlayer spaces from 7.675 nm for MgGaAl to 8.909 nm for Ag_MgGaAl and 12.727 nm for Au_MgGaAl, as shown in Table 1. The position of the

diffraction maximum is seldom varying with the nature of the cation, since the distance in the layer is depending on fitting the cations in the octahedral cage defined by six hydroxyl groups [19,33]. The local lack of order or deformations issued in the brucite-like sheet are due to discrepancies in the ordered arrangement of the octahedral units and promoted the overlap of (110) and (113) peaks for Ag_MgGaAl and Au_MgGaAl. As consequence, the characteristics of the diffraction patterns of Ag_MgGaAl and Au_MgGaAl demonstrate the reconstruction of the LDH structure, but further points out that this procedure may affect the ordering inside the layers leading to the formation of the structural defects. The intensity of the peaks due to (015) and (018) reflections further indicate the distortion of the layered structure. The "*a*" and "*c*" structural parameters [17,31] were calculated as: a = 2 × d (110) and c = 3 × d (006), where d (110) and d (006) are given by the Bragg relation and presented in Table 1. The increases of parameter "*c*" indicate the different nature of anions in Ag_MgGaAl and Au_MgGaAl, and agrees well to the previously reported values for the LDH containing CH_3COO^- and SO_4^{2-} in the interlayers, as previously reported [33,34].

Table 1. The XRD structural characteristics of the MgGaAl based catalysts.

Sample	d (*003*) nm	d (*110*) nm	*a* nm	*c* nm
MgGaAl	7.675	1.538	3.076	23.026
Ag_MgGaAl	8.909	1.536	3.072	26.728
Au_MgGaAl	12.727	1.533	3.066	38.180

Characteristic reflections of gold or silver phases are not observed in the XRD patterns of Ag_MgGaAl and Au_MgGaAl catalysts. This can be due to the small sizes and/or the low content of Au and Ag nanoparticles. Hence, to promote the growing of the small sizes nanoparticles and to study them by XRD, we further calcinated the heterostructured samples at 870 °C. After the calcination, the XRD patterns of the heterostructures (see Figure 1b) show the formation of $MgGa_2O_4$ (denoted with ◊ in Figure 1b) though further reveal the specific reflections of the face-centered cubic (fcc) of Ag (denoted with (▲) in Figure 1b), namely (111), (200) and (220) (JCPDS data no. 04-0783) and the diffraction lines of the (111) and (200) planes of (fcc) of Au (JCPDS Card No. 65-2870), denoted with (△) in Figure 1b.

Next, we used FT-IR analysis to get information about the nature of the anions of the LDH structure. The FT-IR spectra of the catalysts (see Figure 2) resemble those of the LDH phases [33,35]. Typical of all spectra are the strong broad absorbance band between 3600 and 3200 cm^{-1} associated with the stretching mode of the hydroxyl groups, both from the brucite-like layers and the interlayer water molecules, as well as, the water molecules physisorbed on the external surface of the crystallites [36]. For MgGaAl, the ν3 mode of interlayer carbonate is responsible for the intense band at 1384 cm^{-1}. This is a degenerated mode for the D3h symmetry of the original carbonate anion. However, it can be noticed that the band at 1384 cm^{-1} shows a clearly identified shoulder at 1491 cm^{-1}, which can be considered a result of the splitting of the ν3 mode [37]. The replacement of carbonate anions by acetate anions in Au_MgGaAl and by sulphate anions in Ag_MgGaAl is clearly disclosed by FT-IR analysis. For Au_MgGaAl, the bands at 1575 and 1410 cm^{-1} indicate the presence of acetate anions, after the reconstruction; for Ag_MgGaAl, the peak around 1110 cm^{-1} reveal the presence of the SO_4^{2-} in the interlayers. Weaker bands below 1000 cm^{-1} correspond mainly to vibration of lattice bonds of Me–OH while the characteristic peak at 668 cm^{-1} is due to the vibration of the Me−O−Me bonds associated with the cations of the LDH layers [36].
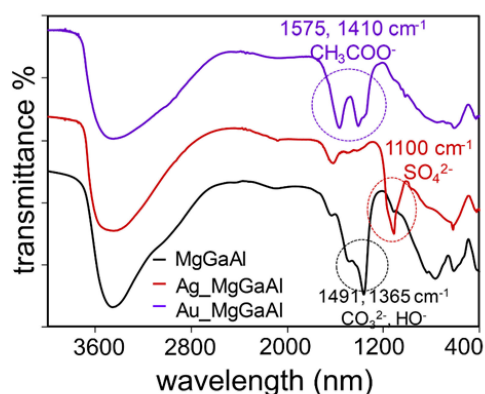
Figure 2. FT-IR spectra of MgGaAl, Ag_MgGaAl and Au_MgGaAl.

2.2. Morphology and Composition Analyses

The morphology and crystalline features of the as-prepared catalysts were investigated by HRTEM and HAADF STEM images, as shown in Figure 3a–k. The results indicate that Ag_MgGaAl and Au_MgGaAl were composed by small nanoparticles, with a relatively narrow size, that are randomly distributed on the larger nanoparticles of the LDH, as shown by TEM images in Figure 3a,c. For both Ag_MgGaAl and Au_MgGaAl, almost spherical dark spots defined by an average size less than 20 nm are clearly seen on the larger nanoparticles of MgGaAl (av. size ~130 nm).
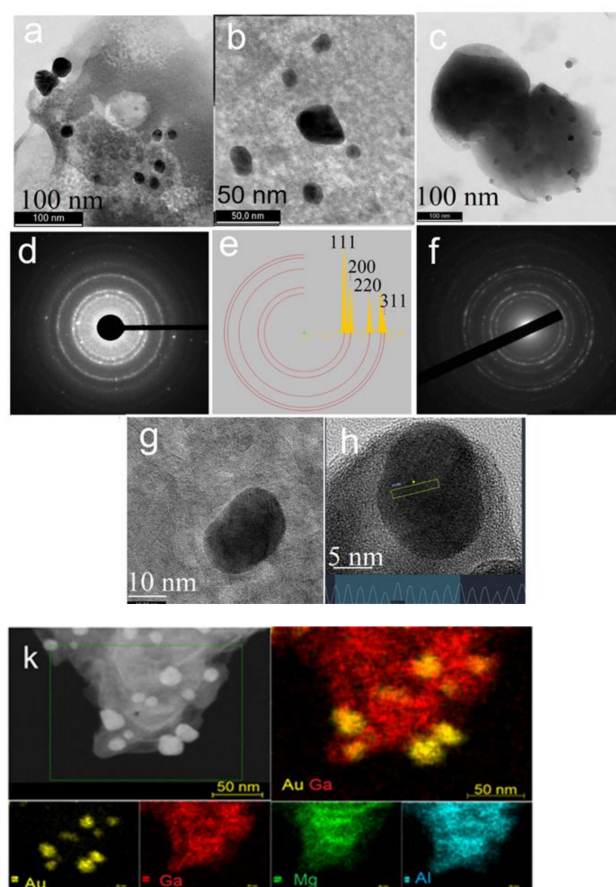

Figure 3. (**a**) TEM image of Au_MgGaAl; (**b**) Higher magnification of TEM image of Au_MgGaAl; (**c**) low magnification TEM image of Ag_MgGaAl; (**d**,**e**) SAED pattern of Au_MgGaAl; (**f**) SAED pattern of Ag_MgGaAl; (**g**) HRTEM image of Ag_MgGaAl; (**h**) HRTEM image of a single nanoparticle on Au_MgGaAl with identification of the crystal plane of gold; (**k**) HAADF STEM image of Au_MgGaAl and the corresponding STEM-EDS element maps.

Notably, HRTEM and SAED images in Figure 3b,d–k clearly identified Au and Ag nanoparticles that are well crystalized with lattice fringes defined by an interplanar spacing of 0.24 and 0.27 nm, respectively. This corresponds to the face-centered cubic (fcc) structure of Au (111) planes and Ag (111), being consistent with the SAED patterns [38]. The typical selected area electron diffraction (SAED) patterns display bright circular rings, featuring a complex pattern in which the diffraction rings of gold (see Figure 3d,e) and silver (Figure 3f), where (1 1 1), (2 0 0), (2 2 0) and (3 1 1) planes of Au and Ag, respectively are combined with the set of the diffraction pattern derived from the LDH [34]. These results demonstrate that in the heterostructured catalysts nanoparticles of Au and Ag, with an average size lower than 20 nm are in close conjunction [37] with the MgGaAl matrix. In addition, high-angle annular dark-field scanning transmission electron microscopy (HAADF-STEM) was employed to analyze the element distribution in Ag_MgGaAl and Au_MgGaAl heterostructures. The elemental mapping by energy-dispersive spectroscopy (EDS) was performed under STEM and we present the EDS map of Au_MgGaAl in Figure 3k. Results confirm that Mg, Ga, and Al are uniformly distributed over the entire catalysts, while Au is dispersed on the catalysts surface. In addition, the EDS analysis (see Supplementary Figure S1) indicates that Au and Ag content of the catalysts are 3.8 wt% for Au in Au_MgGaAl and 3.5 wt% for Ag in Ag_MgGaAl, which is close to the calculated content for the synthesis.

2.3. Optical Characteristics and Plasmonic Response

The formation of the plasmonic metals-LDH heterostructures was further tracked by analyzing the optical behavior of Ag_MgGaAl and Au_MgGaAl by UVDR analysis and the results are shown in Figure 4. The absorption edge of MgGaAl lies in the low UV region while the heterostructured catalysts reveal enhanced absorption in the visible range due to the LSPR response of plasmonic silver and gold. For Au_MgGaAl, the peak with a maximum at 550 nm is attributed to the SPR band of well dispersed nanoparticles of Au. It originates from the intraband excitation of electrons in the outer orbital (6sp) of the Au species and confirms the production of energized electrons [38,39]. For Ag_MgGaAl, the broad peak at 360–600 nm is assigned to the plasmonic response of silver, covering all the visible range. Moreover, the absorption bands of the calcined catalysts displayed higher intensity in comparison to the as-synthesized ones. This can be a consequence of the increase of the nanoparticle size during the calcination process [40–42].
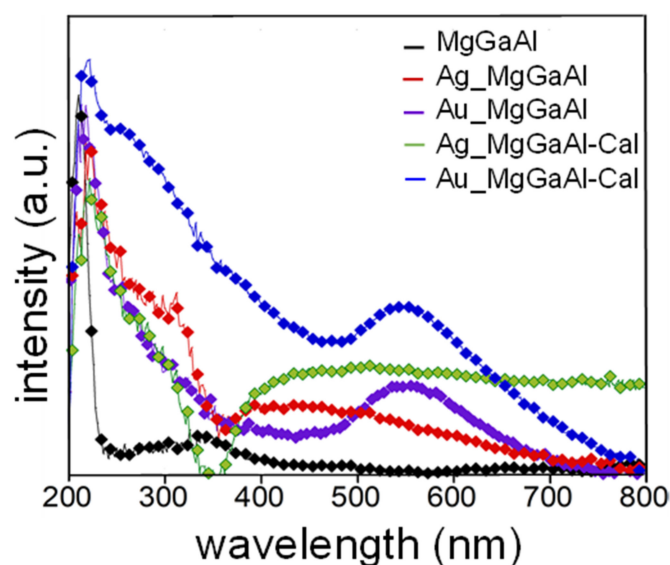

Figure 4. UVDR spectra of the studied photocatalysts.

2.4. XPS Analysis

The surface state of gold and silver in the heterostructured catalysts was explored by XPS analysis and the corresponding spectra are shown in Figure 5.
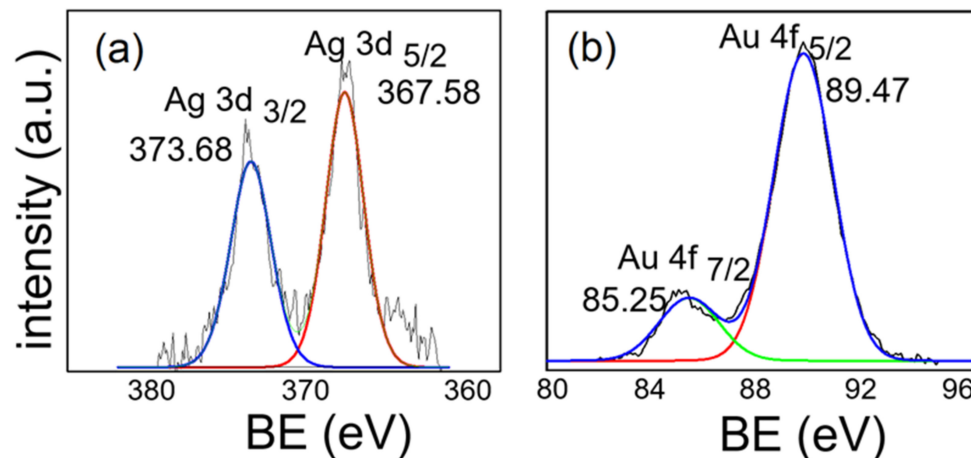

Figure 5. High-resolution XPS spectra of (**a**) Ag3d in Ag_MgGaAl; (**b**) Au4f in Au_MgGaAl.

The peaks at 373.68 and 367.58 eV, associated to Ag 3d 3/2 and Ag 3d 5/2 transitions, respectively (see Figure 5a), indicate that on the surface of Ag_MgGaAl silver is present as Ag^0. This is supported by the fact that the formation of silver nanoparticles was achieved under light that promoted the reduction of Ag^+ to Ag^0 [43]. The state of gold nanoparticles is described by the peaks at 85.25 and 89.47 eV in Figure 5b, which come from Au4f 7/2 and Au 4f 5/2 transitions, respectively, revealing the presence of a mixed states of $Au^{\delta+}$ (δ = 1, 1, 3) on the surface of Au_MgGaAl [44–46]. In both heterostructures, the signals generated by gallium (Supplementary Figure S2) formed peaks at 1145.2 eV and 1118 eV, revealing the presence of Ga 2p 1/2 and Ga 2p 3/2 as Ga^{3+} cations in the LDH layer.

2.5. Photocatalytic Performance in 2-PNh and 2-DCB Photodegradation in Aqueous Solutions

The photocatalytic activity of the plasmonic catalysts was evaluated in the photodegradation of 4-NPh and p-DCB. The characteristic absorptions of 4-NPh at 390 nm and p-DCB at 220 nm were used to monitor the photocatalytic degradation process [47]. Among the examined catalysts, Ag_MgGaAl exhibited the best performance, completely decomposing the tested pollutants. As shown in Figure 6a,b for Ag_MgGaAl, the main adsorption peaks of the pollutants decreased gradually as solar irradiation proceeded, such that the peak almost vanished after 90 min for p-DCB while for 4-NPh the corresponding peak vanished after 360 min.

Figure 7 presents the effective mineralization of 4-NPh (Figure 7i) and 2-DCB (Figure 7ii) evaluated by TOC measurements for the catalysts irradiated by solar and UV light. Firstly, it reveals that the studied catalysts have not been active when irradiated by UV light. This clearly reveals the role of plasmonic characteristics in harvesting the light energy to promote photocatalysis. Thus, under solar light the presence of silver in Ag_MgGaAl highly increased the TOC removal up to 87% as compared to Au_MgGaAl, which mineralized only 71% of 4-NPh in the same experimental conditions. Further, the degradation of 2-DCB Ag_MgGaAl showed the strongest photocatalytic activity under solar irradiation while, almost no photodegradation was achieved under UV irradiation. Thus, the photocatalytic activity of the tested catalysts followed the orders Ag_MgGaAl > Au_MgGaAl > Ag_MgGaAlcal > Au_MgGaAlcal with degradation efficiencies of 2-DCB calculated to be 91%, 76%, 61% and 47% respectively, after 90 min of irradiation with solar light. MgGaAl was not active for the degradation of 2-DCB, while the degradation efficiency for 4-NPh reached only 11% on the LDH precursor. These results reveal the essential roles of the plasmonic responses on promoting the photons harvesting from the visible range of solar light and promoting pollutant degradation [48], but further disclose that

the silver-based photocatalyst led to the best performance. This can be due to the much wider plasmonic peak of nanosilver that points out that Ag_MgGaAl is able to harvest light over a more extended visible light-responsive range in comparison to Au_MgGaAl [49]. The excellent activity of the Ag_MgGaAl sample was a good reason to test the performance of this photocatalyst using a mixture of 4-NPh and p-DCB (1/1 molar ratio).
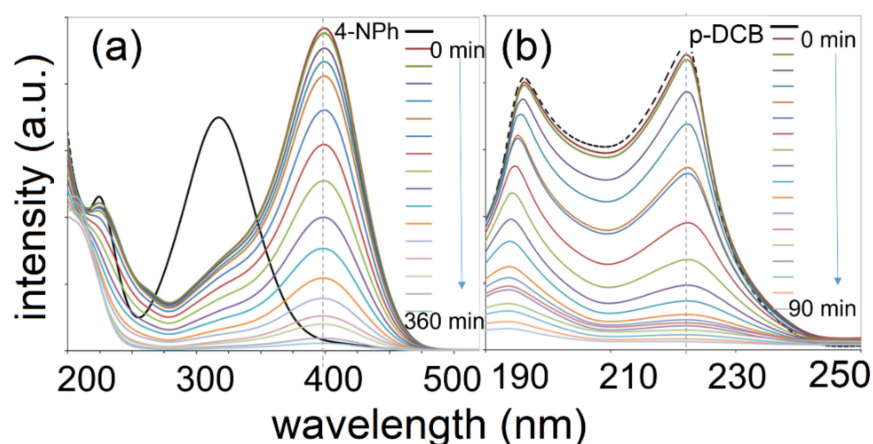

Figure 6. UV−vis absorption spectra of (**a**) 4-NPh; and (**b**) p-DCB solutions in the presence of Ag_MgGaAl and solar irradiation.
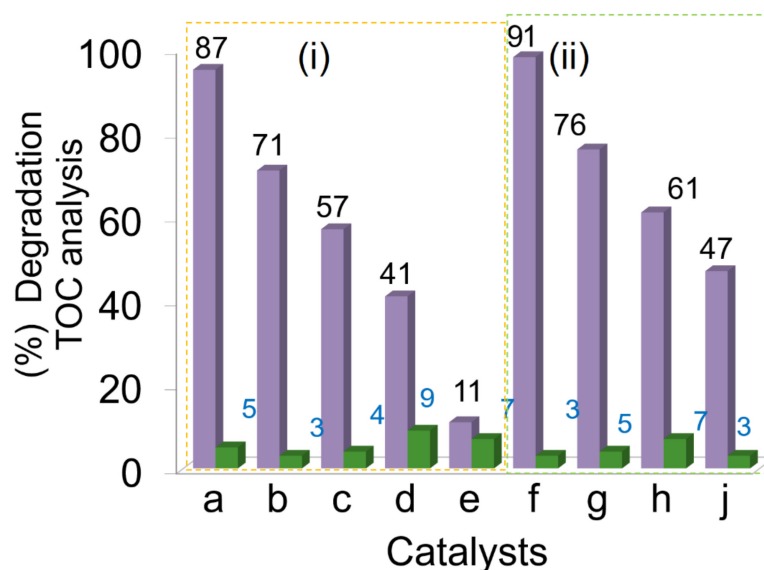

Figure 7. Photocatalytic performance evaluated by TOC measurements for (**i**) 4-NPh removal, after 360 min of irradiation, shown as: (a) Ag_MgGaAl; (b) Au_MgGaAl; (c) Ag_MgGaAcal; (d) Au_MgGaAlcal; (e) MgGaAl; (**ii**) p-DCB removal after 100 min of irradiation for: (f) Ag_MgGaAl; (g) Au_MgGaAl; (h) Ag_MgGaAlcal (j) Au_MgGaAl, by (▬) solar and (▬) UV light.

For 4-NPh (see Figure 8a) a delay of about 120 min was noticed for 4-NPh when found in the mixture of the pollutants. Thus, after 360 min the mixture exposed to the photocatalyst reveal a degradation yield of 75% of 4-NPh after 360 min of irradiation by solar light. This reveals a competition between the pollutants for the adsorption sites or for the HO· radicals involved in the photocatalytic process. On the other hand, p-DCB shows a different degradation profile (Figure 8b), with a fast degradation fitting a Langmuir type allure. After this, the degradation was quite slow, reaching almost 50% after 360 min of irradiation. The different behavior further points out that in their aqueous mixture p-DCB is highly preferred to 4-NPh in the adsorption process in the beginning of irradiation by solar light.
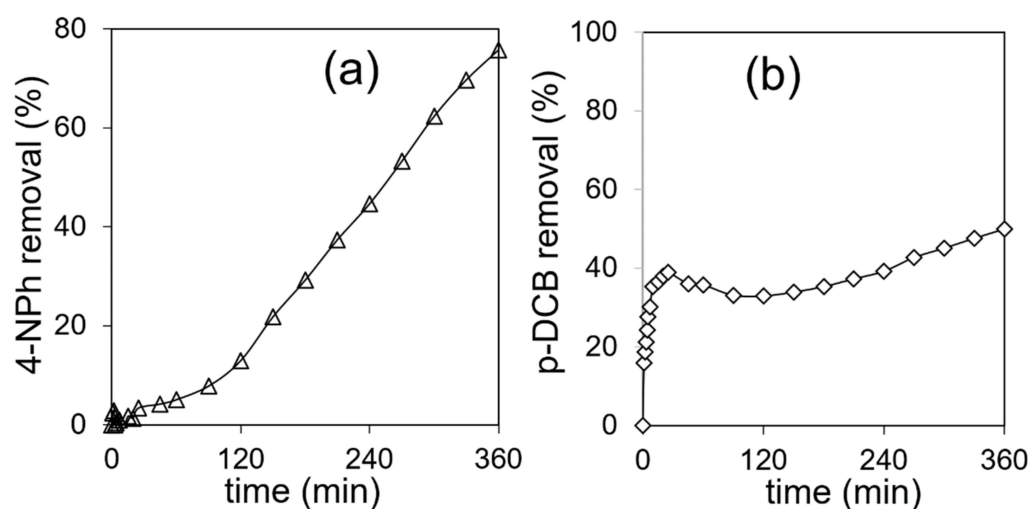
Figure 8. Pollutant % removal of: (**a**) 4-NPh; and (**b**) p-DCB from an aqueous solution containing both pollutants on Ag_MgGaAl.

The reusability of the catalysts was investigated via cycle experiments using a Ag_MgGaAl hybrid photocatalyst. For each test, the reusability of Ag_MgGaAl was evaluated by successive addition of the pollutants such that, before each cycle, the concentration of 4-NPh and p-DCB was equal to 0.125 mmol/L for each. As exhibited in Figure 9, there was just a slight decrease after testing three times, indicating that Ag_MgGaAl can be considered to be a stable and recyclable photocatalyst for the degradation of 4-NPh and p-DCB, respectively.
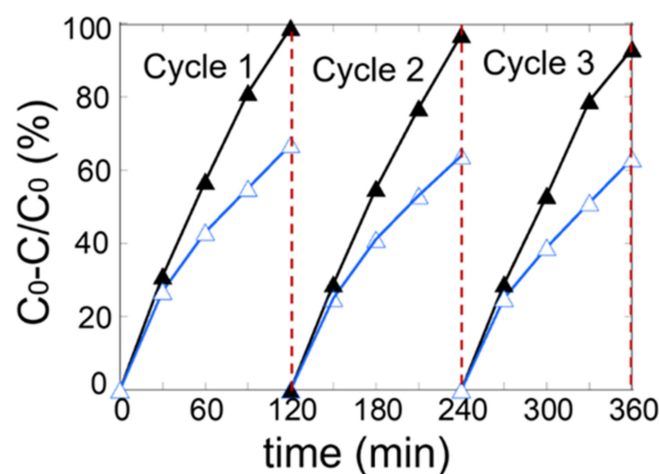

Figure 9. Recycling of Ag_MgGaAl photocatalyst for 4-NPh (Δ) and p-DCB (▲) degradation.

Information about the reactive species formed during the degradation of 4-NPh was obtained by using quenchers, such as isopropanol, that acts as efficient radical scavengers for •OH and benzoquinone, which is acting as an $O_2\bullet^-$ radical scavenger [37,48]. The results are given in Supplementary Figure S3 and show that in the presence of isopropanol the TOC removal (%) of 4-NPh decreased from 87% to 51%, pointing out that •OH radicals act as major reactive species in the photocatalytic system. Further, when benzoquinone was added to trap $O_2\bullet^-$, an obvious inhibition of degradation process was observed, from 87% to 59%, revealing that the addition of benzoquinone decreased the amount of involved $O_2\bullet^-$ during the degradation process. Based on these results, the possible photocatalytic mechanism for the degradation of the studied pollutants is illustrated in Scheme 1 where the pollutants are denoted as Ar-X. It describes that, under solar irradiation, nanoparticles of silver have given rise to photogenerated electron–hole pairs and, some of the photogenerated electrons at the CB of the plasmonic silver could be transferred

to the CB of the LDH, due to the more negative CB position of the LDH than that of nanosilver [50]. Thus, the dissolved oxygen formed $\bullet O_2^-$ radicals, and then further $\bullet OH$ by combining with H_2O. These are preliminary results regarding the mechanism of the studied photocatalytic degradation and will be explored further in future work.
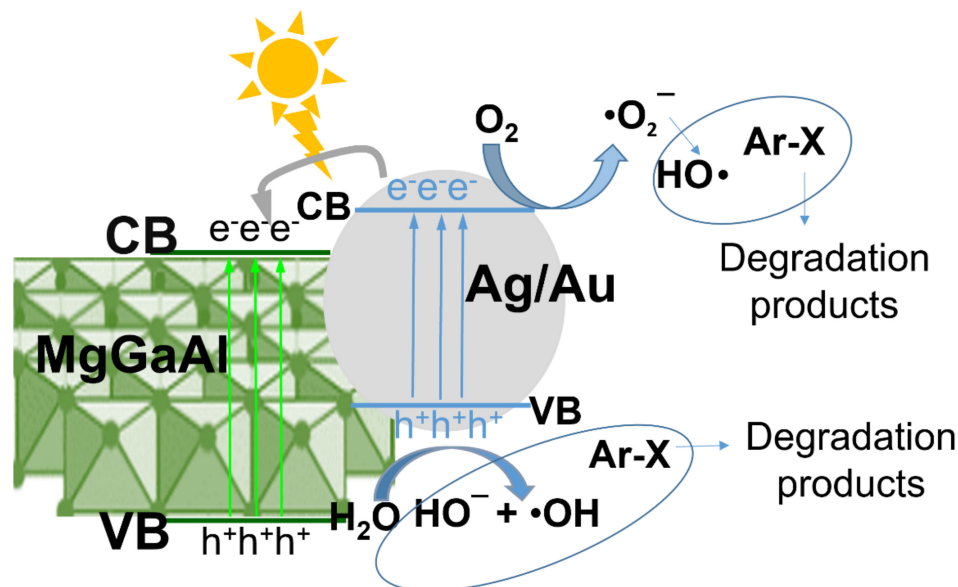
Scheme 1. Possible photocatalytic mechanism for the pollutant's degradation.

Next, we used the experimental data fitting to the pseudo-first, pseudo-second, Weber intraparticle diffusion and Elovich kinetic models, which were used to further investigate the kinetics of the photodegradation of 4-NPh, p-DCB and their mixture, under solar light. Each data set was fitted to the above-described models and the accuracy of the proposed models and the corresponding correlation coefficients are described in Figure 10 and Table 2. The kinetic analysis reveals that the pseudo-first order model fits relatively well when just one pollutant is present in the aqueous solution. As shown by the conversion data presented in Figure 8, the reaction rate increased almost six times for p-DCB degradation in comparison to that of 4-NPh degradation. Therefore, when the pollutants are mixed together, the pseudo-first order model is almost acceptable to fit the data concerning 4-NPh degradation (R^2 = 0.8245), while for p-DCB degradation, the pseudo-second order model fits the decomposition of p-DCB in the mixture with 4-NPh. However, to point out the above proposed kinetic models we present in Figure 10a,b the linear fit for all the systems describing the pseudo-first and pseudo-second order kinetics. Furthermore, the Weber intraparticle diffusion model [51] was chosen to highlight the influence of the intraparticle diffusion on the reaction rate, considering that the adsorption on the photocatalyst surface of the transformed species is a key step of the process, and results are shown in Figure 10c. If data fitted to a linear plot defined as qt versus $t^{0.5}$ with the plot passing through the origin, the intraparticle diffusion is the only rate-controlling step [45]. In the case of our reactions, the plots contain two linear portions for the conversion of p-DCB, alone or mixed with 4-NPh. This reveals that there is more than one rate-controlling step; thus, the adsorption of p-DCB occurs by weaker binding on the photocatalyst surface, followed by the oxidation through the HO radicals, while the ionic structure of the 4-NPh could favor binding forces through electrostatic attraction with the catalysts. Moreover, the deactivating effect the nitro group exerted on the aromatic ring might contribute to a certain inertia of this molecule in the oxidation step. We further reveal that the Elovich model did not fit for any of the studied catalysts because there are no linear dependencies between ln t and qt, as shown by results in Figure 10d hence, the α and β parameters were not calculated for this model.
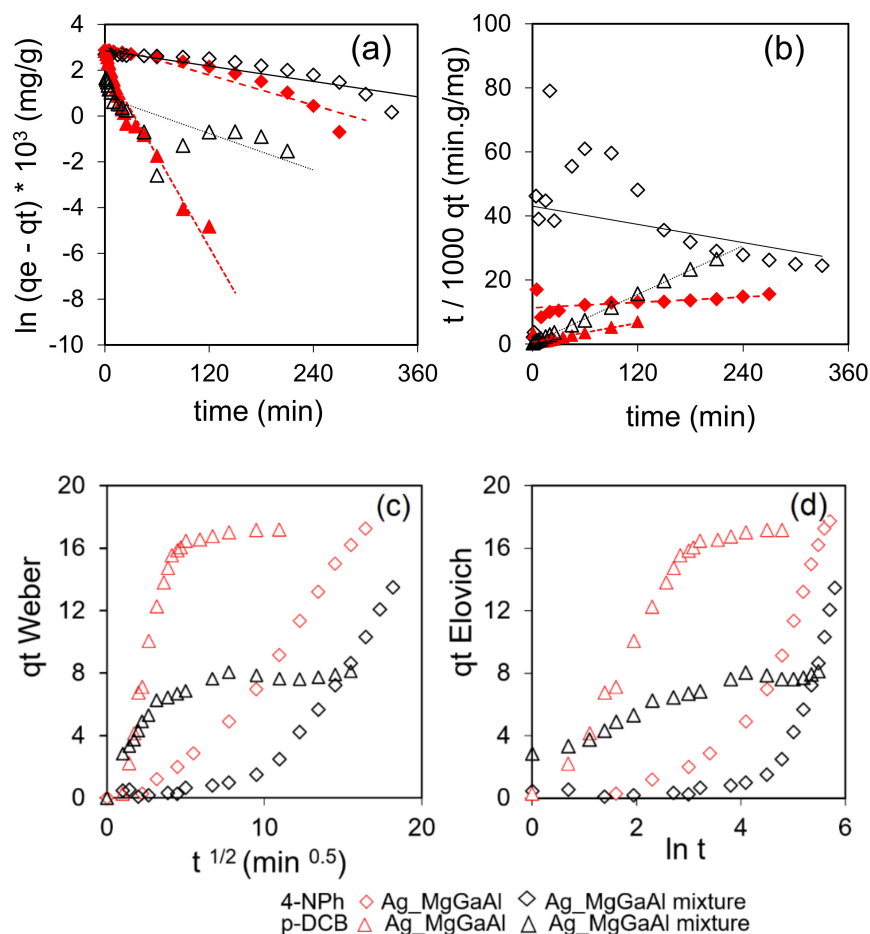
Figure 10. Kinetic analysis as fitted to: (**a**) pseudo-first order; (**b**) pseudo-second order; (**c**) Weber intraparticle diffusion; (**d**) Elovich kinetic models.

Table 2. Kinetic parameters and the correlation coefficients R^2.

Reaction System		Ag_MgGaAl_4-NPh	Ag_MgGaAl_4-NPh (Mix)	Ag_MgGaAl_p-DCB	Ag_MgGaAl_p-DCB (Mix)
Pseudo-first order	k_1	0.011	0.0056	0.0665	0.0133
	R^2	0.9019	0.8245	0.9435	0.5288
Pseudo-second order	k_2	0.0014	0.0046	0.0044	0.0112
	R^2	0.292	0.0773	0.8294	0.9994
Weber intraparticle diffusion	k_{id}	1.1821	-	4.412	1.6169
	C	−1.407	-	−2.422	1.1056
	R^2	0.9862	-	0.9478 *	0.9904 *

* calculated for the first linear range.

3. Materials and Methods

3.1. Fabrication and Characterization of the Catalysts

Ga partially substituted hydrotalcite defined by a M^{2+}/M^{3+} ratio of 2 (where M^{2+} = Mg^{2+} and M^{3+} = Al^{3+} and Ga^{3+}), are obtained by a standard co-precipitation method at a constant pH [13,15] and denoted as MgGaAl. More precisely, the aqueous solutions of $Mg(NO_3)_2\cdot 6H_2O$, $Al(NO_3)_3\cdot 9H_2O$ and $GaSO_4\cdot 7H_2O$ were added to a solution of $Na_2CO_3/NaOH$ at a constant pH of 9.5 and the precipitate was aged for 24 h at 45 °C. Further, after the calcination at 550 °C for 8 h, the evolved mixed oxides were denoted as MgGaAlcal. Heterostructures of the LDH with plasmonic Au and Ag was achieved in aqueous medium during the structural reconstruction of the LDHs, in the aqueous solutions of $Au(CH_3COO)_3$ and Ag_2SO_4, respectively, at room temperature [33,40] and Au and Ag mass content were calculated to reach ~4.0% mass loading.

The heterostructured catalysts were denoted as Au_MgGaAl and Ag_MgGaAl, respectively. After calcination at 550 °C for 8 h the derived catalysts were denoted as Au_MgGaAlcal and Ag_MgGaAlcal.

X-ray diffractions were performed on a PANalytical X'Pert ((Malvern PANalytical Ltd., Almelo, The Netherlands) PROMPD diffractometer equipped with a filtered Cu Kα radiation; measurements were done in the 2θ mode using a bracket sample holder with a scanning speed of 0.04°/4 s in continuous mode. Diffuse Reflectance Infrared Fourier Transform spectra (DRIFT) were measured on a Nicolet 6700 FT-IR spectrometer (Thermo, Waltham, MA, USA), equipped with a mid-IR source (400–4000 cm^{-1}), a KBr-beam splitter and about 200 scans were taken with a 4 cm^{-1} resolution. TEM/HRTEM images and results were obtained on Ultra-High resolution TEM microscope, UHR-TEM-Libra 200 MC/Carl Zeiss GmbH (Carl Zeiss Microscopy GmbH, Oberkochen, Germany). X-ray photoelectron spectroscopy (XPS, PerkinElmer Inc., Waltham, MA, USA) spectra were recorded using a Perkin-Elmer Model 5500-MT spectrometer equipped with Mg Kα radiation (1253.6 eV), operating at 15 kV and 20 mA; the binding energies (BE) were corrected by referencing the C1s peak to 284.8 eV. The UV-vis analysis profiles were acquired with a Jasco 500 UV-vis spectrophotometer within the wavelength range of 200–800 nm.

3.2. Photocatalytic Experiments

The photocatalytic activity of the LDH, the heterostructured catalysts and the calcined derivates were tested for the photodegradation of 4-NPh and 2 DCP in aqueous solutions. For this, appropriate amounts of catalyst powder were dispersed in the pollutant solution with the initial concentration of 0.025 g/L (of single or mol/mol mixture of pollutants) and a solid/liquid ration at 1 g/L. The solutions were stirred in the dark in order to realize the adsorption–desorption equilibrium between the catalytic surface and the pollutants, until no modification of the UV-vis absorption spectra was observed. Afterwards, the catalyst/pollutants mixtures were irradiated using an UNNASOL US 800 solar simulator, using a Xenon Lamp as a light source reaching 870 W/m^2, equipped with UV or Vis block filters. The photocatalytic activity of all catalysts was tested under solar and UV irradiation. The reactions were carried out in a 200 mL reactor with water recirculation in order to avoid the evaporation and to keep the system at a constant volume and temperature. The pollutants' photodegradation profile was monitored by measuring the UV-Vis absorption spectra and by total organic carbon (TOC). TOC of 4-NPh and 2-DCB aqueous solutions were analyzed with a Shimadzu TOC-VCPH (Shimadzu, Kyoto, Japan) analyzer equipped with a NDIR detector, to evaluate the mineralization degree of the organic material. The TOC values were obtained by subtracting IC (inorganic carbon) values from TC (total carbon) values. Removal yield (%) was calculated as: $100 \times (Ao - At)/Ao$, where *Ao* and *At* were the absorbance values measured on solutions taken before the illumination (counted at time zero value) and at time *t* from irradiation start, respectively.

The r kinetics analysis was studied by fitting the experimental data on four models: pseudo-first-order model, pseudo-second-order model, Weber intraparticle diffusion model and Elovich model. The corresponding equations and significance of the calculated parameters are given in Table 3.

Table 3. Equations of the kinetic models applied in this study.

Model	Equation	Parameters Significance and Defining Relations
Pseudo-first order	$\ln(q_e - q_t) = \ln q_e - k_1 t$	$q_e = V(C_o - C_e)/m$; $q_t = V(C_o - C_t)/m$
Pseudo-second order	$t/q_t = 1/(k_2 q_e^2) + t/q_e$	q_e and q_t—measured species at equilibrium and time t; V—volume of solution; m—adsorbent weight; k_1, k_2—rate constant for pseudo-first and pseudo-second order; k_{id}—rate constant for intraparticle diffusion;
Weber diffusion	$q_t = k_{id} \, t^{0.5} + C$	
Elovich	$q_t = 1/\beta \, (\ln \alpha\beta) + 1/\beta \ln t$	α—initial adsorption rate; β—desorption constant

4. Conclusions

We have successfully achieved to obtain novel plasmonic heterostructures by the close conjunction of plasmonic metals, specifically Au and Ag nanoparticles and gallium partially substituted hydrotalcite layered matrix. The catalysts were obtained by a facile synthesis procedure, via calcination-reconstruction of MgGaAl in the solutions of gold acetate and silver sulphate, respectively. The analysis of photocatalytic degradation of 4-NPh and 2-DCB from aqueous solutions, under irradiation by solar light, revealed that the plasmonic behavior of the newly designed catalysts plays a key role in establishing high photocatalytic performances for the removal of the studied pollutants from the aqueous mediums.

Supplementary Materials: The following supporting information can be downloaded at: https://www.mdpi.com/article/10.3390/catal12111351/s1, Figure S1: EDS analysis for (a) Ag_MgGaAl and (b) Au_MgGaAl catalysts; Figure S2: High resolution XPS spectra of Ga2p in both Ag_MgGaAl and Au_MgGaAl catalysts. Figure S3: Effect of different scavengers on the degradation of 4-NP in the presence of Ag-MgGaAl.

References

1. Available online: https://www.dw.com/en/water-scarcity-eu-countries-forced-to-restrict-drinking-water-access/a-62363819 (accessed on 27 July 2022).
2. Available online: https://www.statista.com/chart/26140/water-stress-projections-global/ (accessed on 21 July 2022).
3. Lin, L.; Jiang, W.; Chen, L.; Xu, P.; Wang, H. Treatment of produced water with photocatalysis: Recent advances, affecting factors and future research prospects. *Catalysts* **2020**, *10*, 924. [CrossRef]
4. Zimmerman, J.B.; Anastas, P.T.; Erythropel, H.C.; Leitner, W. Designing for a green chemistry future. *Science* **2020**, *367*, 397–400. [CrossRef] [PubMed]
5. Murgolo, S.; De Ceglie, C.; Di Iaconi, C.; Mascolo, G. Novel TiO$_2$-based catalysts employed in photocatalysis and photoelectrocatalysis for effective degradation of pharmaceuticals (PhACs) in water: A short review. *Curr. Opin. Green Sustain. Chem.* **2020**, *30*, 100473. [CrossRef]
6. Dong, H.; Zeng, G.; Tang, L.; Fan, C.; Zhang, C.; He, X.; He, Y. An overview on limitations of TiO$_2$-based particles for photocatalytic degradation of organic pollutants and the corresponding countermeasures. *Water Res.* **2015**, *79*, 128–146. [CrossRef] [PubMed]
7. Marcu, I.C.; Pavel, O.D. Layered Double Hydroxide-Based Catalytic Materials for Sustainable Processes. *Catalysts* **2022**, *12*, 816. [CrossRef]
8. Liu, C.; Mao, S.; Shi, M.; Wang, F.; Xia, M.; Chen, Q.; Ju, X. Peroxymonosulfate activation through 2D/2D Z-scheme CoAl-LDH/BiOBr photocatalyst under visible light for ciprofloxacin degradation. *J. Hazard. Mater.* **2021**, *420*, 126613. [CrossRef]
9. Brongersma, M.L.; Halas, N.J.; Nordlander, P. Plasmon-induced hot carrier science and technology. *Nat. Nanotechnol.* **2015**, *10*, 25–34. [CrossRef]
10. Liu, C.; Mao, S.; Shi, M.; Hong, X.; Wang, D.; Wang, F.; Xia, M.; Chen, Q. Enhanced photocatalytic degradation performance of BiVO4/BiOBr through combining fermi level alteration and oxygen defect engineering. *Chem. Eng. J.* **2022**, *449*, 137757. [CrossRef]
11. Chen, Y.; Wang, Y.; Li, W.; Yang, Q.; Hou, Q.; Wei, L.; Liu, L.; Huang, F.; Ju, M. Enhancement of photocatalytic performance with the use of noble-metal-decorated TiO$_2$ nanocrystals as highly active catalysts for aerobic oxidation under visible-light irradiation. *Appl. Catal. B Environ.* **2017**, *210*, 352–367. [CrossRef]
12. Zhang, G.; Zhang, X.; Meng, Y.; Pan, G.; Ni, Z.; Xia, S. Layered double hydroxides-based photocatalysts and visible-light driven photodegradation of organic pollutants: A review. *Chem. Eng. J.* **2020**, *392*, 123684. [CrossRef]
13. Li, C.; Wei, M.; Evans, D.G.; Duan, X. Layered double hydroxide-Based nanomaterials as highly efficient catalysts and adsorbents. *Small* **2014**, *10*, 4469–4486. [CrossRef]

14. Puscasu, C.-M.; Seftel, E.M.; Mertens, M.; Cool, P.; Carja, G. ZnTiLDH and the Derived Mixed Oxides as Mesoporous Nanoarchitectonics with Photocatalytic Capabilities. *J. Inorg. Organomet. Polym. Mater.* **2014**, *25*, 259–266. [CrossRef]

15. Mohapatra, L.; Parida, K. A review on the recent progress, challenges and perspective of layered double hydroxides as promising photocatalysts. *J. Mater. Chem. A* **2016**, *4*, 10744–10766. [CrossRef]

16. Du, H.; Fan, J.; Miao, C.; Gao, M.; Liu, Y.; Li, D.; Feng, J. Recent advances in constructing interfacial active catalysts based on layered double hydroxides and their catalytic mechanisms. *Trans. Tianjin Univ.* **2021**, *27*, 24–41. [CrossRef]

17. Gu, Z.; Atherton, J.J.; Xu, Z.P. Hierarchical layered double hydroxide nanocomposites: Structure, synthesis and applications. *Chem. Comm.* **2015**, *51*, 3024–3036. [CrossRef]

18. Wu, M.J.; Wu, J.Z.; Zhang, J.; Chen, H.; Zhou, J.Z.; Qian, G.R.; Xu, Z.P.; Du, Z.; Rao, Q.L. A review on fabricating heterostructures from layered double hydroxides for enhanced photocatalytic activities. *Catal. Sci. Technol.* **2018**, *8*, 1207–1228. [CrossRef]

19. Ng, S.F.; Lau, M.Y.L.; Ong, W.J. Engineering layered double hydroxide–based photocatalysts toward artificial photosynthesis: State-of-the-Art progress and prospects. *Solar RRL* **2021**, *5*, 2000535. [CrossRef]

20. Prasad, C.; Tang, H.; Liu, Q.Q.; Zulfiqar, S.; Shah, S.; Bahadur, I. An overview of semiconductors/layered double hydroxides composites: Properties, synthesis, photocatalytic and photoelectrochemical applications. *J. Mol. Liq.* **2019**, *289*, 111114. [CrossRef]

21. Li, Z.; Chen, M.; Hu, H.; Zhang, Q.; Tao, D. Mechanochemical synthesis of novel Pt modified ZnAl-LDH for effective ciprofloxacin photodegradation. *J. Solid State Chem.* **2020**, *290*, 121594. [CrossRef]

22. Li, Z.; Zhang, Q.; Liu, X.; Wu, L.; Hu, H.; Zhao, Y. One-step mechanochemical synthesis of plasmonic Ag/Zn–Al LDH with excellent photocatalytic activity. *J. Mater. Sci.* **2018**, *53*, 12795–12806. [CrossRef]

23. Espinal, R.; Taboada, E.; Molins, E.; Chimentao, R.J.; Medina, F.; Llorca, J. Ethanol steam reforming over hydrotalcite-derived Co catalysts doped with Pt and Rh. *Top. Catal.* **2013**, *56*, 1660–1671. [CrossRef]

24. Liu, D.; Barbar, A.; Najam, T.; Javed, M.S.; Shen, J.; Tsiakaras, P.; Cai, X. Single noble metal atoms doped 2D materials for catalysis. *Appl. Catal. B Environ.* **2021**, *297*, 120389. [CrossRef]

25. Katsumata, K.I.; Sakai, K.; Ikeda, K.; Carja, G.; Matsushita, N.; Okada, K. Preparation and photocatalytic reduction of CO_2 on noble metal (Pt, Pd, Au) loaded Zn–Cr layered double hydroxides. *Mat. Lett.* **2013**, *107*, 138–140. [CrossRef]

26. Zhang, Z.; Li, P.; Zhang, X.; Hu, C.; Li, Y.; Yu, B.; Zeng, N.; Lv, C.; Song, J.; Li, M. Recent advances in layered-double-hydroxides based noble metal nanoparticles efficient electrocatalysts. *Nanomaterials* **2021**, *11*, 2644. [CrossRef] [PubMed]

27. Tsyganok, A.I.; Inaba, M.; Tsunoda, T.; Uchida, K.; Suzuki, K.; Takehira, K.; Hayakawa, T. Rational design of Mg–Al mixed oxide-supported bimetallic catalysts for dry reforming of methane. *Appl. Catal. A Gen.* **2005**, *292*, 328–343. [CrossRef]

28. Lestari, P.R.; Takei, T.; Yanagida, S.; Kumada, N. Facile and controllable synthesis of Zn-Al layered double hydroxide/silver hybrid by exfoliation process and its plasmonic photocatalytic activity of phenol degradation. *Mater. Chem. Phys.* **2020**, *250*, 122988. [CrossRef]

29. Bates, N. Mothball poisoning. *Emerg. Nurse* **2002**, *10*, 24–28. [CrossRef]

30. Weidman, E.K.; Tsiouris, A.J.; Heier, L.A. Toxic encephalopathy due to paradichlorobenzene toxicity: A case report and review of imaging characteristics. *Clin. Imaging* **2015**, *39*, 1095–1098. [CrossRef]

31. Evans, D.G.; Slade, R.C. Structural aspects of layered double hydroxides. In *Layered Double Hydroxides*; Xue, D., Evans, G.D., Eds.; Springer: Berlin, Germany, 2006; pp. 1–87.

32. Braterman, P.S.; Xu, Z.P.; Yarberry, F. Layered Double Hydroxides (LDHs). In *Handbook of Layered Materials*; Auerbach, S.M., Carrado, K.A., Dutta, P.K., Marcel, D., Eds.; Marcel Dekker, Inc.: New York, NY, USA, 2004; Chapter 8; pp. 363–457.

33. Gilea, D.; Radu, T.; Muresanu, M.; Carja, G. Plasmonic photocatalysts based on silver nanoparticles-Layered double hydroxides for efficient removal of toxic compounds using solar light. *Appl. Surf. Sci.* **2018**, *444*, 407–413. [CrossRef]

34. Mikami, G.; Grosu, F.; Kawamura, S.; Yoshida, Y.; Carja, G.; Izumi, Y. Harnessing self-Supported Au nanoparticles on layered double hydroxides comprising Zn and Al for enhanced phenol decomposition under solar light. *Appl. Catal. B Environ.* **2016**, *199*, 260–271. [CrossRef]

35. Govindappa, M.; Farheen, H.; Chandrappa, C.P.; Rai, R.V.; Raghavendra, V.B. Mycosynthesis of silver nanoparticles using extract of endophytic fungi, Penicillium species of Glycosmis mauritiana, and its antioxidant, antimicrobial, anti-inflammatory and tyrokinase inhibitory activity. *Adv. Natur. Sci. Nanosci. Nanotechnol.* **2016**, *7*, 035014. [CrossRef]

36. Gomes, J.F.; Garcia, A.C.; Gasparotto, L.H.S.; De Souza, N.E.; Ferreira, E.B.; Pires, C.; Tremiliosi-Filho, G. Influence of silver on the glycerol electro-oxidation over AuAg/C catalysts in alkaline medium: A cyclic voltammetry and in situ FTIR spectroscopy study. *Electrochim. Acta* **2014**, *144*, 361–368. [CrossRef]

37. Liu, C.; Mao, S.; Wang, H.; Wu, Y.; Wang, F.; Xia, M.; Chen, Q. Peroxymonosulfate-assisted for facilitating photocatalytic degradation performance of 2D/2D WO3/BiOBr S-scheme heterojunction. *Chem. Eng. J.* **2022**, *430*, 132806. [CrossRef]

38. Furube, A.; Du, L.; Hara, K.; Katoh, R.; Tachiya, M. Ultrafast Plasmon-Induced Electron Transfer from Gold Nanodots into TiO2 Nanoparticles. *J. Am. Chem. Soc.* **2007**, *129*, 14852–14853. [CrossRef]

39. Kominami, H.; Tanaka, A.; Hashimoto, K. Mineralization of organic acids in aqueous suspensions of gold nanoparticles supported on cerium (iv) oxide powder under visible light irradiation. *Chem. Commun.* **2010**, *46*, 1287–1289. [CrossRef]

40. Carja, G.; Birsanu, M.; Okada, K.; Garcia, H. Composite plasmonic gold/layered double hydroxides and derived mixed oxides as novel photocatalysts for hydrogen generation under solar irradiation. *J. Mater. Chem. A* **2013**, *1*, 9092–9098. [CrossRef]

41. Lin, C.H.; Chu, H.L.; Hwang, W.S.; Wang, M.C.; Ko, H.H. Synthesis and optical properties of Mg-Al layered double hydroxides precursor powders. *AIP Adv.* **2017**, *7*, 125005. [CrossRef]

42. Al-Sarraj, A.; Saoud, K.M.; Elmel, A.; Mansour, S.; Haik, Y. Optoelectronic properties of highly porous silver oxide thin film. *SN Appl. Sci.* **2021**, *3*, 15. [CrossRef]

43. Wu, Y.; Lin, Y.; Xu, J. Synthesis of Ag–Ho, Ag–Sm, Ag–Zn, Ag–Cu, Ag–Cs, Ag–Zr, Ag–Er, Ag–Y and Ag–Co metal organic nanoparticles for UV-Vis-NIR wide-range bio-tissue imaging. *Photochem. Photobiol. Sci.* **2019**, *18*, 1081–1091. [CrossRef]

44. Klyushin, A.Y.; Rocha, T.C.; Hävecker, M.; Knop-Gericke, A.; Schlögl, R. A near ambient pressure XPS study of Au oxidation. *Phys. Chem. Chem. Phys.* **2014**, *16*, 7881–7886. [CrossRef]

45. Pramanik, G.; Humpolickova, J.; Valenta, J.; Kundu, P.; Bals, S.; Bour, P.; Dracinsky, M.; Cigler, P. Gold nanoclusters with bright near-Infrared photoluminescence. *Nanoscale* **2018**, *10*, 3792–3798. [CrossRef] [PubMed]

46. Peters, S.; Peredkov, S.; Neeb, M.; Eberhardt, W.; Al-Hada, M. Size-dependent XPS spectra of small supported Au-Clusters. *Surf. Sci.* **2013**, *608*, 129–134. [CrossRef]

47. Chen, H.; Yang, M.; Tao, S.; Chen, G. Oxygen vacancy enhanced catalytic activity of reduced Co_3O_4 towards p-nitrophenol reduction. *Appl. Catal. B Environ.* **2017**, *209*, 648–656. [CrossRef]

48. Chen, Y.; Li, W.; Wang, J.; Yang, Q.; Hou, Q.; Ju, M. Gold nanoparticles-modified TiO_2/SBA-15 nanocomposites as active plasmonic photocatalysts for the selective oxidation of aromatic alcohols. *RSC Adv.* **2016**, *6*, 70352–70363. [CrossRef]

49. Gu, S.; Lu, Y.; Kaiser, J.; Albrecht, M.; Ballauff, M. Kinetic analysis of the reduction of 4-nitrophenol catalyzed by Au/Pd nanoalloys immobilized in spherical polyelectrolyte brushes. *Phys. Chem. Chem. Phys.* **2015**, *17*, 28137–28143. [CrossRef]

50. Seftel, E.M.; Puscasu, M.; Mertens, M.; Cool, P.; Carja, G. Photo-responsive behavior of γ-Fe2O3 NPs embedded into ZnAlFe-LDH matrices and their catalytic efficiency in wastewater remediation. *Catal. Today* **2015**, *252*, 7–13. [CrossRef]

51. Cai, J.; Chen, C.R.; Zeng, H.Y.; Yi, M.Y.; Xiao, G.F.; Zhu, R.L.; Cao, X.J.; Shen, S.-G.; Peng, J.W. Fabrication of Ag2O/Ag decorated ZnAl-Layered double hydroxide with enhanced visible light photocatalytic activity for tetracycline degradation. *Ecotoxicol. Environ. Saf.* **2019**, *172*, 423–431.